Martensitic transformation, magnetic and magnetocaloric properties of Ni-Mn-Fe-Sn Heusler ribbons

A. Deltell, Abd El-Moez A.Mohamed, P. Álvarez-Alonso, M. Ipatov, J.P. Andrés, J.A. González, T. Sánchez-Fernández, A. Zhukov, M.L. Escoda, J.J. Suñol, R. López Antón

PII: S2238-7854(21)00276-3

DOI: https://doi.org/10.1016/j.jmrt.2021.03.049

Reference: JMRTEC 2890

To appear in: *Journal of Materials Research and Technology*

Received Date: 16 October 2020

Revised Date: 8 March 2021

Accepted Date: 14 March 2021

Please cite this article as: Deltell A, El-Moez A.Mohamed A, Álvarez-Alonso P, Ipatov M, Andrés JP, González JA, Sánchez-Fernández T, Zhukov A, Escoda ML, Suñol JJ, López Antón R, Martensitic transformation, magnetic and magnetocaloric properties of Ni-Mn-Fe-Sn Heusler ribbons, *Journal of Materials Research and Technology*, https://doi.org/10.1016/j.jmrt.2021.03.049.

Martensitic transformation, magnetic and magnetocaloric properties of Ni-Mn-Fe-Sn Heusler ribbons

A. Deltell[a], Abd El-Moez A.Mohamed[b,c], P. Álvarez-Alonso[d], M. Ipatov[e,f], J.P. Andrés[g], J.A. González[g], T. Sánchez-Fernández[d], A. Zhukov[e,f,h], M.L. Escoda[a], J.J. Suñol[a], R. López Antón[g,1]

[a] *Physics Department, University of Girona, 17073 Girona, Spain.*
[b] *Department of Physics, Faculty of Science, University of Sohag, 82524 Sohag, Egypt*
[c] *School of Metallurgy and Materials, University of Birmingham, Birmingham B15 2TT, United Kingdom*
[d] *Physics Department, University of Oviedo, 33007 Oviedo, Spain*
[e] *Department of Materials Physics, Faculty of Chemistry, University of the Basque Country, 20018 San Sebastián, Spain*
[f] *Department of Applied Physics I, EUPDS, University of the Basque Country, 20018 San Sebastian, Spain*
[g] *Instituto Regional de Investigación Científica Aplicada (IRICA) and Departament of Applied Physics,University of Castilla-La Mancha, 13071 Ciudad Real, Spain*
[h] *IKERBASQUE, Basque Foundation for Science, 48011 Bilbao, Spain*

Abstract

Melt-spun ribbons of nominal composition$Ni_{50}Mn_{36-x}Fe_xSn_{14}$ (x = 0, 2, and 3) were prepared by melt-spinning. The alloys undergo a martensitic transformation from $L2_1$ austenite to an orthorhombic 4O martensite on cooling, as determined by X-ray powder diffraction analysis. Replacement of Mn by Fe linearly reduces the characteristic temperatures of the martensitic transformation (the equilibrium temperature decreases from 328 to 285 K) and reduces the Curie temperature of the austenite phase (from 336 to 300 K), whereas the effect of the applied magnetic field on the martensite transition temperatures is negligible. Magnetic measurements (zero-field cooled, ZFC, and field cooled, FC, curves, AC susceptibility measurements) hint the coexistence of two different ferromagnetic martensitic magnetic phases. Moreover, the AC susceptibility measurements and the irreversibility of the ZFC and FC curves point towards the presence of antiferromagnetic and ferromagnetic interactions in the martensitic phase. All samples exhibit spontaneous exchange bias at 2 K, with double-shifted loops, whereas the evolution of the conventional exchange bias with the temperature agrees quite well with the behavior of ferromagnetic regions surrounded by spin-glass regions or with the coexistence of ferromagnetic-antiferromagnetic interactions. $Ni_{50}Mn_{36-x}Fe_xSn_{14}$ ribbons present a moderate inverse magnetocaloric effect (with a maximum of the magnetic entropy change of 5.7 $Jkg^{-1}K^{-1}$ for $\mu_0 H$ = 3 T for x = 3). It is worth to note that these materials feature a significant reservoir (up to 44 $Jkg^{-1}K^{-1}$ for x = 2) of magnetic entropy change, linked to the proximity of the austenitic ferromagnetic transition to the martensitic transformation.

Keywords: Ferromagnetic shape memory alloys; melt-spun ribbons; exchange bias; magnetic entropy change.

[1] Corresponding author. Email: ricardo.lopez@uclm.es

1. Introduction

Since the report of large magnetic-field-induced strain in nonstoichiometric Ni_2MnGa compounds associated with the magnetic-field-driven martensitic microstructure rearrangement [1], ferromagnetic shape memory alloys (FSMAs) have triggered great attention for their great utilization potential in applications, such as magnetic actuators and sensors [1,2]. Among the FSMAs, off-stoichiometric Ni-Mn-X (X = In, Sn, and Sb) shape memory alloys present multifunctional properties around the martensitic transformation, such as tuneable metamagnetic shape memory effect with composition [3], exchange bias [4] and caloric effects [5–7].

The exchange bias, EB, manifests as a shift of the magnetic hysteresis loop along the field axis after cooling down under an applied magnetic field, and occurs when two materials with fairly different magnetic anisotropy are exchange-coupled at their interface, being usually one ferromagnetic (FM) and the other antiferromagnetic (AFM), although it can also be observed with other exchange coupled systems (e.g., FM/ferrimagnetic, spin-glass/FM…) [4,8]. In particular, in Ni-Mn-based Heusler FSMA, the exchange interaction is related to the distance Mn-Mn, where Mn atoms in regular sites of the unit cell are FM coupled, while excess Mn atoms occupying Ni or X sites are antiferromagnetically coupled to Mn atoms at regular sites [9]. Recently, Wang et al. [10]. reported the spontaneous exchange bias effect (SEB) after zero-field-cooled (ZFC) process from a demagnetized state in Ni-Mn-In bulk alloys. Authors attributed this phenomenon to a superferromagnetic unidirectional anisotropy formed isothermally through a tunnelling superexchange between superparamagnetic domains embedded in an AFM matrix. On the other hand, Z.D. Han et al. [11] attribute the SEB in Ni-Mn-Ga alloys to the irreversible growth of FM domains changing from non-percolating to percolating state, forming the unidirectional anisotropy at the interface of ferromagnetic domains dispersed in a spin glass matrix. As can be seen, a generally accepted interpretation of the SEB effect is still under discussion.

Among the caloric effects, the magnetocaloric effect (MCE) is the most widely investigated. It consists of the variation of the isothermal magnetic entropy and adiabatic temperature changes produced by variations of the applied magnetic field. The so-called Metamagnetic Shape Memory Alloys (MSMAs) Ni-Mn-based Heusler alloys exhibit an inverse MCE associated with the martensitic transformation [12], since the magnetic moment of martensite is lower than in austenite as a result of a preponderance of the Mn-Mn antiferromagnetic coupling in the cubic phase [13]. Besides, the alloys present a conventional MCE at the austenite ferromagnetic-to-paramagnetic phase transition, a feature that can be used to double the cooling capacity [14].

In this manuscript we investigate the effect of the Fe-doping on the EB and MCE. The addition of a fourth element is a common strategy that seeks to improve the magnetic properties of Ni-Mn-Sn alloys; for instance, Ni substitution by Co or Fe around 1-3 at. % in $Ni_{50-x}(Fe\text{-}Co)_xMn_{37}Sn_{13}$ increases the magnetocaloric effect. The entropy change for 3 at. % Fe in this composition reaches 30 $Jkg^{-1}K^{-1}$ at $\mu_0\Delta H = 5$ T, a fairly high value compared to 20 $Jkg^{-1}K^{-1}$ obtained in the ternary alloy [15,16]. In addition, doping alters the martensitic and magnetic phase transitions. In this sense, it has been shown that Co addition increases the Curie temperature (T_C) in $Ni_{50-x}Co_xMn_{38}Sn_{12}$ [17,18]. Ni replacement by Fe in $Ni_{50-x}Fe_xMn_{40}Sn_{10}$ increases both the austenite and martensite unit cell volumes, as well as tends to increase the transformation volume, $\Delta V/V$, above 1 %

[19]. Replacing Mn by Fe in $Ni_{50}Mn_{37-x}Fe_xSn_{13}$ and $Ni_{50}Mn_{36-x}Fe_xSn_{14}$ alloys enlarges the Curie temperature of the austenitic phase [20]. A similar behaviour is noticed in $Ni_{50}Mn_{40-x}Fe_xSn_{10}$, although replacing Mn by Fe above 3 % leads to the precipitation of a second phase (Fe γ-phase) accompanied by a decrease of the martensitic characteristic temperatures [21]. It has been found that the presence of a γ-phase enlarges the ductility of Ni-Mn-based Heusler alloys [22], although Fe-doped $Ni_{50-x}Fe_xMn_{39}Sn_{11}$ single-phase alloy exhibits an enhanced ductility as well.

The fabrication process of Ni-Mn-based FSMA in bulk requires a subsequent extended heat treatment [23], as well as in powder form, in which case a compaction step is also needed. Rapid solidification by melt-spinning technique circumvents any ulterior fabrication process to obtain homogeneous, high chemical ordering and single-phase polycrystalline materials. Besides, this method offers several advantages with respect to other fabrication processes: (a) the ribbon geometry is well suited to develop magnetocaloric materials because ensures a heat diffusion characteristic length (i.e., large surface with a thickness of a few microns) that allows a good heat transfer to the heat transfer fluid in a magnetocaloric device [24]; (b) it is common to observe an improvement of the magnetocaloric properties with respect to the materials presented in other forms [25]; (c) melt-spun ribbons are more adequate for certain practical applications due to their mechanical properties and demagnetization effect, negligible if the magnetization is performed along the longitudinal direction.

This paper provides a profound analysis of the influence of the magnetic field and the Mn replacement by Fe in $Ni_{50}Mn_{36}Sn_{14}$ melt-spun ribbon FSMA on structural and magnetic phase transitions, as well as on magnetic and magnetocaloric properties. In particular, both spontaneous and conventional EB are discerned for all specimens, accompanied by a shift of the martensitic transformations with Fe-content. The magnetic entropy change, on the other hand, increases appreciably. Finally, we discuss the dependence of the total entropy change of the martensitic transformation with the proximity of both martensitic and magnetic transformations.

2. Experimental procedure

$Ni_{50}Mn_{36-x}Fe_xSn_{14}$, with x = 0, 2, and 3 (hereafter referenced as Fe0, Fe2, and Fe3) master alloys were arc-melted (Bühler MAM-1) in argon atmosphere from highly pure elements (> 99.98 %, supplied by Sigma-Aldrich). The ingots were remelted several times to ensure chemical homogeneity. As-quenched melt-spun ribbons were obtained using an Edmund Bühler model SC melt spinner system at a linear speed of the rotating copper wheel of 48 m/s in an argon atmosphere.

The ribbons morphology was investigated by scanning electron microscopy (SEM), using a model DSM-960A Zeiss microscope, operating at 20 kV, equipped with an energy dispersive X-ray spectrometry (EDX) unit. X−ray powder diffraction (XRD) patterns of ribbon flakes were collected on a Bruker D8 Advance diffractometer in a Bragg Brentano configuration using Cu−Kα radiation (λ_{Cu} = 0.15406 nm). The XRD patterns were analyzed using the software developed at the UdG. Thermal analysis was carried out by differential scanning calorimetry (DSC) in a TA instrument DSC Q2000 at heating/cooling rates of 10 K/min under Ar atmosphere. Magnetic characterization was performed in a Quantum Design PPMS device. The magnetic field was applied along the ribbons axis to minimize the demagnetizing field. AC magnetic susceptibility was measured under a magnetic field of 1 mT in the temperature range of 5 K to 350 K with

a temperature rate of 5 K/min. Magnetization versus temperature $M(T)$ curves following the ZFC, FC, and field heating (FH) protocols were collected under a constant magnetic field in the range 5 mT - 3 T.

3. Results and discussion

3.1. Morphology

Figure 1(a) reproduces the cross-section fracture morphology for the samples. In all the micrographs, the upper surface of the tape is the ribbon free surface, whereas the lower part is the ribbon face in contact with the melt-spinning wheel. The average thicknesses of the ribbons are 15, 25, and 18 µm for Fe0, Fe2, and Fe3, respectively, with an estimated error of 1 µm. All ribbons exhibit a similar columnar structure aligned perpendicular to the ribbon plane with a thin layer of grains near the ribbon wheel side. The grain growth towards the free-surface results from the temperature gradient, a consequence of the large heat transfer from the ribbon to the wheel, as reported in the literature [26]. This is consistent with the observed mechanically fragility of the ribbon flakes, especially along the direction of columnar grains growth [9]. The EDX microanalysis shows the homogeneous distribution of the chemical composition in the ribbons. The average values are listed in Table 1 (with an accuracy of 0.5 at. %), evidencing a certain reduction of Mn as compared with the nominal composition, although it is negligible for the discussion that follows. It is noteworthy that neither the EDX nor the backscattering analysis have revealed the occurrence of secondary phases, which have been reported in other Fe-doped Ni-Mn-Sn alloys, like the γ phase detected in $Ni_{50-x}Fe_xMn_{38}Sn_{12}$ and $Ni_{50-x}Fe_xMn_{39}Sn_{11}$ [27,28].

3.2. Martensitic transformation

DSC curves (see Figure 2) display the features of a first-order reversible martensitic transformation (MT) for the studied samples, Fe0, Fe2, and Fe3, i.e., endothermic and exothermic peaks at temperatures T_A and T_M, corresponding to the reverse and forward MT respectively, which occur with moderate hysteresis ΔT (defined as $\Delta T = T_A - T_M$) of 12-15 K (see Table 2). These values are similar to those previously reported in $Ni_{50}Mn_{50-x}Sn_x$, $Ni_{50-x}Fe_xMn_{40}Sn_{10}$ and $Ni_{46-x}Fe_xMn_{43}Sn_{11}$ ribbons [19,29,30], but lower than in $Ni_{50.3}Mn_{35.5}Sn_{14.4}$ ribbons [31]. Characteristic transition temperatures, i.e., the starting and finishing martensite and austenite temperatures, T_{MS}, T_{MF}, T_{AS}, T_{AF}, were determined as the intersection of the tangents of each peak with the baseline. These results are summarized in Table 2, as well as the thermodynamic equilibrium temperatures [defined as $T_0 = 0.5(T_A+T_M)$]. In particular, T_0 decreases linearly with the increase of Fe-content (about -15 K per Fe at. %). In $Ni_{50}Mn_{36}Sn_{14}$ bulk, it has been reported that the characteristic T_{MS}, T_{MF}, T_{AS}, T_{AF} temperatures are 220, 210, 240, and 250 K respectively [32].

The crystal structure of the ribbons was determined from conventional X-ray powder diffraction. Figure 3 depicts XRD diffractograms collected for the three specimens (flakes) at 350 K (iron free) and 295 K (Fe2 and Fe3) to determine the austenite crystal structure. The Miller indices of the main Bragg reflections are also plotted to help the reader to identify the phases; the diffraction peaks belonging to the minor martensite and sample holder phases are indicated by 4O and SH respectively. The $Ni_{50}Mn_{36}Sn_{14}$ and $Ni_{50}Mn_{33}Sn_{14}Fe_3$ ribbons present the $L2_1$ austenite phase. Note the existence of uneven Miller indexes like (111), whereas both $L2_1$ austenite and orthorhombic 4O (Pmma space group) martensite phases are present in $Ni_{50}Mn_{34}Sn_{14}Fe_2$ ribbons [15,33],

in agreement with the DSC thermograms. Note also that the austenite is the preponderant phase for the Fe2 specimen, as expected since the XRD pattern was collected for the as-received ribbons.

In Figure 4, the XRD diffractograms for the ribbons at 150 K (well below T_{MF}) are plotted. As expected, the patterns correspond to the orthorhombic 4O martensite, with no traces of secondary phases, except for the properly defined sample holder, which is coherent with the microanalysis results (see previous subsection). It has been reported that the reduction of the MT temperatures is related to the reduction of the electron valence concentration (e/a) or the increment of the lattice volume [34]. Electron valence concentration, cell parameters and cell volume for the martensitic (4O) and austenitic ($L2_1$) structures are summarized in Table 1. The decrease of the structural transformation temperature as we increase Fe content has been experimentally related to a) the diminution of the e/a parameter ,associated with the electrons in the outer cells [16], and b) the slight augment of unit cell volume due to the larger atomic size of Fe [35]. From first-principles investigations, it has been found that antiferromagnetic/ferromagnetic competition is the underlying responsible for the martensitic transition [36], with the AFM (FM) stabilizing the martensite (austenite) phase. In this context, the variations of electron valence concentration would affect the magnetic interactions of the atoms in the cell and therefore the martensitic transformation. The doping elements such as Fe alter the AFM/FM stability favoring the relative structure stability of the ferromagnetic state compared with the antiferromagnetic state; in particular, T_M decreases with the Mn content reduction [37]. No significant changes occur for the lattice parameters after replacing Mn by Fe, in contrast to the regular increment reported for replacing Ni by Fe [19]. Crystallographic data also show that the volume of the martensitic cell is similar to that of the austenitic cell, although the increment of the Fe-content leads to a reduction of the transformation volume, $\Delta V/V = (V_M - V_A)/V_A$ (see Table 1).

3.3. Magnetic properties

Magnetization curves measured under an applied magnetic field of 5 mT and 3 T, following the three standard thermal protocols (i.e., ZFC-FC-FH) for the samples, are shown in Figure 5. Focusing on the curves measured at 5 mT, we can observe some shared traits for all samples. Hence, at 400 K, the specimens are in the austenitic phase in the paramagnetic state, and hence almost-zero magnetization. At the temperatures corresponding to the MT, a peak in the magnetization is expected. However, that peak is very weak and we observe it only in the Fe0 sample after amplifying the graph, as can be observed in the inset of figure 5. In that inset, we can see how the magnetization increases as we approach the Curie temperature, T_C^A, and just below that, the magnetization displays a hysteretic transformation at temperatures compatible with the MT obtained from the DSC measurements. In the case of the other two samples, that peak corresponding to the MT is masked by the increase of the magnetization found at about 300 K (see below). Pathak et al [38] found that in the case of the $Ni_{50}Mn_{36.5}In_{13.5}$ Heusler alloy, the martensitic transition evolves from a PM austenitic phase to a PM martensitic one. Although there are some similarities with our case, such as a very small peak due to the MT at low fields, increasing strongly as the applied field is increased, there are other differences, e.g., different slopes of the inverse of the susceptibility before and after the TM (not shown in the article), which seem to discard that

explanation for our samples. On cooling, the magnetization increases at about 300 K, giving rise to a small plateau, and increasing strongly again at about 220-250 K. This kind of plateau, observed at low fields, have been linked previously to the coexistence of two magnetic phases with different Curie temperatures [39] in Ni-Mn-Ga Heusler alloys. Xuan et al. [40] also observed a similar plateau in Ni-Mn-Sn Heusler alloys with high content of Mn, although they did not discuss its origin, and the same happened in the work of Bachaga et al [17] studying $Ni_{50-x}Co_xMn_{38}Sn_{12}$ alloys. Therefore, we can consider two Curie temperatures in the martensitic phase, the one giving rise to the plateau, T_{C1}^{M}, and the one that results in the sharp increase in the magnetization, T_{C2}^{M}. The Curie temperatures were obtained as minima in the first derivative of the magnetization and are gathered in Table 2. However, in the structural characterization there was no evidence of two different martensitic phases. Hence, the appearance of a secondary magnetic phase could be linked to some regions with small local variations in the Mn content , although not associated with changes in the crystal symmetry, inducing changes in the AFM or FM coupling of the Mn atoms. In order to obtain additional information about that magnetic phase, neutron diffraction measurements would be required, given the fact that this technique is sensitive not only to the structure but also to the magnetic order of the materials. Therefore, we are considering it for future works in this system. At lower temperatures, the ZFC splits from the FC and FH curves -with similar level of separation in the three specimens- evidencing the presence of a magnetic irreversibility, which has been linked sometimes to the existence of ferromagnetic particles or grains in a non-magnetic matrix, both in Heusler alloys [41] and in granular alloys [42,43], but also with magnetically inhomogeneous states [23] and, more specifically, with the coexistence of AFM and FM exchange interactions in the martensite [40,44]. This coexistence of AFM and FM exchange interactions can give rise to exchange bias phenomena, as we shall study later on. Note that the magnetization of specimen Fe3 exhibits a peak at T ~ 275 K in the FH curve, a slightly lower temperature than T_{C1}^{M}, most likely being a Hopkinson maximum, as observed in other Ni-Mn-Sn ribbons [23], although the Hopkinson effect has not been detected in either $Ni_{50}Mn_{36}Sn_{14}$ [45] or $Ni_{50-x}Fe_xMn_{36}Sn_{14}$ [46] bulk alloys. Several authors have also attributed such a maximum in the magnetization close to a Curie temperature to the Hopkinson effect in other samples [47–50]. The Hopkinson effect manifests itself by a sharp maximum in the magnetic permeability of a material at a temperature slightly below the Curie Temperature [51,52], usually related with a faster decrease of magnetic anisotropy constant with temperature as compared with the magnetization. Therefore, a peak in the magnetization in a measurement at constant field can be related to the Hopkinson effect.

With regard to the ZFC-FC curves measured under an applied field of 3 T, there are several differences with the ZFC-FC curves obtained under low magnetic field. First of all, a clear peak in the magnetization appears at temperatures consistent with the MT, i.e., the magnetization increases close to the Curie temperature, T_C^{A} and just below that, the magnetization displays a hysteretic transformation at temperatures compatible with the MT obtained from DSC thermograms. As it has been commented before, this peak was only clearly seen in the ZFC-FC curves obtained at low field in the Fe0 sample, and only after magnifying the graph. The values of the MT temperatures have been estimated, using the tangent method, and agree well to the temperatures obtained from

calorimetric data. Secondly, the plateau observed at low field is no longer found, and the irreversibility of the ZFC and FC curves practically vanishes.

Figure 6 plots the heating curves under different applied magnetic field for the sample Fe3. The peak in the temperature dependence of the magnetization indicates the transition from the high-temperature austenite to the low-temperature martensite, as seen previously. It appears in all the curves excepting the one obtained at 5 mT. Note that the characteristic temperatures of the MT keep unchanged with the increment of the magnetic field, as it has been reported by Castillo-Villa et al. [53] and also by Emre et al. [54] in another Heusler alloy, Ni-Mn-Co-Sn system doped with Nb. Additionally, the plateau observed at low field, linked to the coexistence of two magnetic phases, decreases as the applied field increases, practically disappearing at 0.5 - 1 T. This behavior was also reported by Zhukov et al. [39], although in that case it vanished at an even lower applied field (about 0.05 T).

To analyze the magnetic inhomogeneities previously noticed, we carried out AC susceptibility measurements. Figure 7 depicts the temperature dependence of the real part, left, and imaginary part, right, of the AC susceptibility for our samples. Although we measured at different frequencies between 100 Hz and 10 kHz, we only show both extremes for sake of clarity. In the case of the Fe0 samples, there is a hysteretic peak at temperatures corresponding to the MT, agreeing well with the values obtained from the DSC measurements. However, this peak is not observed in the other two samples, exactly what we have commented in the ZFC-FC curves obtained at low magnetic field. Moreover, there is no peak corresponding to the T_C^A, but two clear peaks in the real part of the susceptibility, as can be seen in Figure 7 (left), a smaller one, at 295 K for the sample Fe0 and at 283 K fors samples Fe2 and Fe3, and a bigger one, at 203 K for sample Fe0, 222 K for Fe2, and 236 K for Fe3 sample. Given the similarity to the values of T_{C1}^M and T_{C2}^M determined from the ZFC-FC curves, these peaks would correspond to both T_C^M. However, we should also remark that in the case of the sample Fe3, in the cooling curve measured at 10 kHz, the peak at 283 K is greatly enhanced, likely due to the influence of the Hopkinson effect [47]. Coming back to the lack of peak associated with the MT in the Fe2 and Fe3 samples, the reason for that is, most likely, what we discussed in the ZFC-FC curves: the MT takes place at a temperature relatively close to that of the T_{C1}^M but, alas, its expected peak is fairly smaller than that linked to T_{C1}^M. As we have seen in the case of Fe0, the peak of the MT is about one order of magnitude smaller (take into account the logarithmic representation). Therefore, the peak of the MT is masked by the other one.

In the imaginary part, on the other hand, we can observe those two peaks linked to the Curie temperatures, with the same sample affected by the Hopkinson effect, but also another peak at 150 K for Fe0 and at 130 K for Fe2 and Fe3 samples. This peak is frequency dependent and anhysteretic, and it would be linked to the presence of cluster-like entities of various sizes. Thus, depending on the size of the clusters, there could be a blocking, linked to a ferromagnetic-superparamagnetic transition, or a freezing,as in a spin-glass material, characteristic temperature [5,55]. Given the coexistence of FM and AFM interactions in the Ni-Mn-Sn martensite phases and the presence of two magnetic phases (as discussed previously), both options seem plausible. Considering that temperature tentatively as a freezing temperature, T_f, we can estimate the relative variation in T_f per decade of frequency:

$$\delta = \frac{\Delta T_f}{T_f \Delta(\log f)} \quad (1)$$

which is a quantitative measure of the effect of the frequency on the shift of the peak [55], usually of the real part, although in this case we apply it to the imaginary part. The values that we obtain for our Ni-Mn-Sn-(Fe) ribbons are in the range 0.03-0.04, in between those reported for canonical spin-glass systems, e.g., δ = 0.005 for CuMn, and for ideal noninteracting superparamagnetic systems, δ = 0.1 for Fe nanoparticles in alumina matrix [5]. In fact, our values would correspond to an intermediate situation, the cluster glass regime, as reported by Samanta et al. [56] in the Heusler alloy Ga_2MnCo. Another feature characteristic of spin-glass-like materials is the appearance of a peak in the real part of the AC susceptibility, but our measures only show a small cusp, not clearly defined, at those temperatures. Conversely, sometimes the blocking temperature has associated a peak only in the imaginary part, as can be seen, for instance, in ref. [5]. Furthermore, we have commented that the splitting of the ZFC and FC curves hints the coexistence of AFM and FM interactions, in which case the hypothetical blocking temperature would represent the temperature below which the AFM layer can pin the FM adjacent layer [5], and therefore it can trigger EB phenomena. To check this hypothesis, several hysteresis loops under an applied field up to 5 T at different temperatures were measured after ZFC and FC protocols. In Figure 8 (left) the hysteresis loops measured at 2 K under both ZFC and FC protocols are shown, whereas on the left the evolution of the coercivity, $\mu_0 H_C$, and exchange field, $\mu_0 H_E$, obtained under FC protocol, with temperature is depicted. A clear shift of the loops is observed, even after a ZFC protocol, pinpointing the existence of spontaneous EB in our samples. We should note the different shape of the hysteresis loops depending on the thermal protocol: the loops obtained after FC have the typical shape of a FM material, whereas those obtained after ZFC exhibit a double-shifted hysteresis loop [57], sometimes called “hummingbird-like loops” [58] or “wasp-waist hysteresis loops” [59]. This feature is characterized by a thinner/narrower width of the loop at low fields, which remembers a wasp-waist, or the shape of a hummingbird. This shape is found in quite different systems and sometimes coupled with EB phenomena, for example, when we have two different phases with different coercivities and even with different EB [58]. In the case of Heusler alloys [60,61], it is usually observed in systems with coexistence of AFM-FM coupling in which the AFM phase is divided in two types of regions but locally oriented in opposite directions due to the imprint of the FM phase during the ZFC procedure. When a hysteresis loop is carried out below T_B, each of these regions couples with FM clusters in opposite way, leading to a double-shifted loop. This behavior is also found in some FM/AFM multilayers [62,63].

Focusing on the evolution of coercivity and exchange field, measured under FC protocol, with the temperature, as seen in Figure 8 (right), $\mu_0 H_E$ presents a maximum value at 2 K, the lowest temperature, decreasing monotonically as the temperature increases, and practically vanishing at a certain temperature, about 70 K, well below the T_B found in the AC measurements, whereas the coercivity presents a maximum value at about 60-40 K. This behavior is quite typical when there is coexistence of FM-AFM interactions in Heusler alloys [64–66] or there are FM regions with spin-glass-like regions, observed, e.g., in multilayers systems [67], and also in Heusler alloys [68]. The effect of the addition of Fe on the EB phenomena is quite small in our case. In particular, the maximum value of $\mu_0 H_E$ increases slightly as we add Fe, from 25.8 mT to 26.8 mT,

and, although the temperature at which the EB vanishes is practically the same, about 70 K, the decrease of $\mu_0 H_E$ becomes more abrupt. Noteworthily, the increase of the maximum value of $\mu_0 H_E$ as we increase the Fe content goes parallel to the decrease of the electron valence concentration, contrary to what Pathak et al [66] observed in the case of $Ni_{50}Mn_{35}In_{15-x}Si_x$ Heusler alloys. Additionally, the temperature of the maximum of the coercivity decreases slightly (from 60 to 40 K). This behavior is quite similar to the results found in bulk $Ni_{50}Mn_{36}Sn_{14}$ Heusler alloys doped with Fe by Passamani et al [20], with the main difference that in their case the evolution of the coercivity for the sample without Fe decreased strongly at 50 K (whereas in our case, it reached a maximum at 60 K. Additionally, the values of $\mu_0 H_E$ and $\mu_0 H_C$ are higher in all the cases, probably due to the higher applied magnetic field along the FC protocol (5 T in our case, 2 T in theirs)

3.4. Magnetocaloric effect

Earlier section shows that the replacement of Mn by Fe leads to a shift of the MT to lower temperatures, although the characteristic MT temperatures are kept in the range around room temperature, which makes these alloys potentially interesting for room temperature magnetic refrigeration applications. Moreover, all three alloys exhibit moderate values of thermal hysteresis, also a requirement for magnetic refrigeration. However, these features are not enough for an optimum magnetocaloric material; a large and reversible magnetic entropy change ΔS_{Mag} is also needed. The reversibility of the magnetocaloric effect has been studied in other Heusler alloys [69,70] as well as in other systems, as Fe-Rh alloys [71,72]. In this article we have focused our efforts on analyzing the effect of Fe-addition in Ni-Mn-Sn ribbons on the magnetic entropy change. In this sense, it is well known that the total entropy change linked to the MT, the ΔS^{MT}, represents a limit to the attainable magnetic entropy change, and it has been phenomenologically stablished that ΔS^{MT} decreases exponentially with the increment of the generalized order parameter $T_C^A - T_0$ [3,19]. From such relation, it can be deduced that the closest the Curie temperature of the austenite to the equilibrium temperature, the largest the magnetic entropy change values can be achieved. Therefore, we have calculated the entropy variation from the DSC data for each specimen as $\Delta S_i = \frac{\Delta Q_i}{T_i}$ for the forward, $i = \mathrm{M}$, and reverse transformation, $i = \mathrm{A}$, where ΔQ_i stands for the heat exchanged by the corresponding transformation process and correspond to the area, in absolute value, below the DSC peaks from the forward and inverse transformation. ΔS^{MT} was estimated as the average of the ΔS_M and ΔS_A, as shown in Table 2. The total entropy change of the current ribbons and other shape memory alloys are compared in Figure 9 as a function of the generalized order parameter. As expected from the closeness of the MT and T_C^A, our ribbons present one of the largest values of the total entropy among the ferromagnetic shape memory alloys, which implies a large reservoir of magnetic entropy change. These features motivated us to analyze the magnetocaloric properties of the ribbons; we have estimated the magnetic entropy from the thermomagnetic curves on heating by means of the well-known Maxwell relation:

$$\Delta S_{\mathrm{Mag}}(T,H) = S(T,H) - S(T,0) = \mu_0 \int_0^H \left(\frac{\partial M(T,H')}{\partial T}\right) \mathrm{d}H' \qquad (2)$$

Figure 10 represents the magnetic entropy change of the three Ni-Mn-Sn-(Fe) ribbons obtained from the thermomagnetic curves measured in the ZFC mode at 3 T. Each curve shows a positive, corresponding to an inverse magnetocaloric effect, narrow

peak at $T \sim T_0$ associated with the MT, and two broader negative, i.e., conventional magnetocaloric effect, peaks at T_{C2}^{M} and T_C^{A}, linked to the second-order magnetic phase transitions of the ribbons in the martensite and austenite phase respectively; the second magnetic phase transition observed in the martensite phase has negligible effect on the magnetocaloric response. The inset in Figure 10 plots $\Delta S_{Mag}(T)$ under different applied magnetic fields for the Fe2 ribbons. Comparable results have been obtained for the other ribbons, not shown in the article. Note that the increment of the magnetic field produces an enhancement of both the maximum and width of each peak, but the temperatures at which they occur are not modified, as expected from the observed null effect of the magnetic field on the characteristic temperatures of the MT, as seen in Figure 6. The Fe-doping shifts the positive peak towards lower temperatures, in agreement with the DSC and $M(T)$ data and enlarges the inverse magnetocaloric effect. The maximum magnetic entropy change occurs for the Fe3 sample, reaching up to 5.7 $Jkg^{-1}K^{-1}$ under a magnetic field change of 3 T, similar to the reported values in other Ni-MnSn melt-spun ribbons [19].

The moderate thermal hysteresis of the MT points to a thermoelastic transformation. To confirm this hypothesis, we have determined the enthalpy of the martensitic transformation. When considering it equal to the heat exchanged ΔQ_i, the transformation is assumed as reversible. However, taking into account the accommodation of the modified structures in the form of friction and slip, there should exist a contribution of irreversible dissipated energy W_d. There is another contribution to the enthalpy, as part of the energy can be stored in elastic energy E_{el} related to elastic deformation occurring along with a structural change. Both the irreversibly dissipated energy and the elastically accumulated energy can be evaluated for the forward, $i = \mathrm{M}$, and reverse, $i = \mathrm{A}$, transformation by the following expressions [73]:

$$E_{el,i} = \frac{1}{4}\Delta S_i[(T_{AF} - T_{AS}) + (T_{MS} - T_{MF})] \quad (3)$$

$$W_{d,i} = \frac{1}{2}\Delta S_i[(T_{AF} + T_{AS}) - (T_{MS} + T_{MF})] \quad (4)$$

Thus, the enthalpies of both martensitic and austenitic transformations are determined as $\Delta H_i = \Delta Q_i + E_{el,i} - W_{d,i}$ and are shown in Table 3. The entropy has been calculated by applying the following relationship: $\Delta S_i = \Delta H_i / T_0$ [74]. All the alloys exhibit an irreversibly dissipated energy superior to the energy stored in elastic form. Nonetheless, both values are small and therefore these data confirm that the structural transformations are of thermoelastic type. The alloy with the highest values of enthalpy and entropy variation is Fe2. The variation of heat and enthalpy is similar in martensitic, cooling, and austenitic, heating. This tendency is broken in the Fe2 sample, which presents much higher energy exchanges. This is probably the consequence that the energy stored in the martensitic bonds is greater than in the austenitic ones in this alloy [75]. Also, the austenitic transformations require less energy because, since they are endothermic, this warming contributes to the release and relaxation of internal microstrains.

4. Conclusions

Melt-spun ribbons of nominal composition $Ni_{50}Mn_{36-x}Fe_xSn_{14}$ (x = 0, 2, and 3) prepared by melt-spinning present a martensitic transformation from $L2_1$ austenite to an orthorhombic 4O martensite around room temperature with moderate thermal

hysteresis. Partial replacement of Mn by Fe decreases the temperature of the MT as the Fe content increases, as observed from the DSC data and ZFC-FC-FH thermomagnetic data under a magnetic field of 3 T, with the Curie temperature of the austenite phase also decreasing from 336 to 300 K. The irreversibility below 250 K points out the coexistence of AFM and FM exchange interactions in the martensitic phase. Besides, the ZFC-FC-FH curves at low applied field evidence the presence of two FM martensitic magnetic phases, also pinpointed in the AC susceptibility measurements with two peaks linked to the Curie temperatures of the martensitic magnetic phases in both the real and imaginary parts of the AC susceptibility. A frequency-dependent peak observed at 130-150 K in the imaginary part hints the existence of a blocking temperature whereas a peak linked to the MT is only seen in the real part of the AC susceptibility of the FeO sample. Besides, the evolution of the conventional EB, after FC under a magnetic field of 5 T, with the temperature concurs quite well with ferromagnetic-antiferromagnetic interactions coexisting but also with the behavior of FM regions surrounded by spin-glass regions, whereas the effect of the Fe in the EB properties is almost negligible. The large entropy change driven by the martensitic transformation indicates that these ribbons have a large reservoir of magnetocaloric effect; in this regard, the Ni-Mn-Sn-(Fe) ribbons present moderate values of the magnetic entropy change (up to 5.7 J/kgK for Fe3 for a magnetic field change of 3 T) for small magnetic fields.

Acknowledgements
The support received from the following organizations is gratefully acknowledged: Spanish MINECO, project numbers: MAT2016-75967-P and MCIU-19-RTI2018-094683-B-C52, and Principality of Asturias, project number: IDI/2018/000185. We also thank the enlightening discussions with Prof. B. Hernando.

References

[1] Faran E, Shilo D. Ferromagnetic Shape Memory Alloys—Challenges, Applications, and Experimental Characterization. Exp Tech 2016;40:1005–31. https://doi.org/10.1007/s40799-016-0098-5.
[2] Wilson SA, Jourdain RPJ, Zhang Q, Dorey RA, Bowen CR, Willander M, et al. New materials for micro-scale sensors and actuators. An engineering review. Mater Sci Eng R Reports 2007;56:1–129. https://doi.org/10.1016/j.mser.2007.03.001.
[3] Kainuma R, Oikawa K, Ito W, Sutou Y, Kanomata T, Ishida K. Metamagnetic shape memory effect in NiMn-based Heusler-type alloys. J Mater Chem 2008;18:1837–42. https://doi.org/10.1039/B713947K.
[4] Giri S, Patra M, Majumdar S. Exchange bias effect in alloys and compounds. J Phys Condens Matter 2011;23:073201. https://doi.org/10.1088/0953-8984/23/7/073201.
[5] Chernenko VA, Barandiarán JM, Rodriguez Fernández J, Rojas DP, Gutiérrez J, Lázpita P, et al. Magnetic and magnetocaloric properties of martensitic Ni 2Mn 1.4Sn 0.6 Heusler alloy. J. Magn. Magn. Mater., vol. 324, 2012, p. 3519–23. https://doi.org/10.1016/j.jmmm.2012.02.080.
[6] Sharma J, Suresh KG. Observation of Large Exchange Bias Effect in Bulk Mn50Ni41Sn9 Heusler Alloy. IEEE Trans Magn 2014;50:1–4. https://doi.org/10.1109/TMAG.2014.2325779.
[7] Li Z, Zhang Y, Sanchez-Valdes CF, Sanchez Llamazares JL, Esling C, Zhao X, et al. Giant magnetocaloric effect in melt-spun Ni-Mn-Ga ribbons with magneto- multistructural transformation. Appl Phys Lett 2014;104:044101.

[8] Nogués J, Sort J, Langlais V, Skumryev V, Suriñach S, Muñoz JS, et al. Exchange bias in nanostructures. Phys Rep 2005;422:65–117. https://doi.org/10.1016/j.physrep.2005.08.004.
[9] Hernando B, Sánchez Llamazares JL, Prida VM, Baldomir D, Serantes D, Ilyn M, et al. Magnetocaloric effect in preferentially textured Mn50Ni40In10melt spun ribbons. Appl Phys Lett 2009;94:222502. https://doi.org/10.1063/1.3147875.
[10] Wang BM, Liu Y, Ren P, Xia B, Ruan KB, Yi JB, et al. Large Exchange Bias after Zero-Field Cooling from an Unmagnetized State. Phys Rev Lett 2011;106:077203. https://doi.org/10.1063/1.3686717.
[11] Han ZD, Qian B, Wang DH, Zhang P, Jiang XF, Zhang CL, et al. Magnetic phase separation and exchange bias in off-stoichiometric Ni-Mn-Ga alloys. Appl Phys Lett 2013;103:172403. https://doi.org/10.1063/1.4826654.
[12] Franco V, Blázquez JS, Ipus JJ, Law JY, Moreno-Ramírez LM, Conde A. Magnetocaloric effect: From materials research to refrigeration devices. Prog Mater Sci 2018;93:112–232. https://doi.org/10.1016/j.pmatsci.2017.10.005.
[13] Aksoy S, Acet M, Deen PP, Mañosa L, Planes A. Magnetic correlations in martensitic Ni-Mn-based Heusler shape-memory alloys: Neutron polarization analysis. Phys Rev B 2009;79:212401. https://doi.org/10.1103/PhysRevB.79.212401.
[14] Titov I, Acet M, Farle M, González-Alonso D, Mañosa L, Planes A, et al. Hysteresis effects in the inverse magnetocaloric effect in martensitic Ni-Mn-In and Ni-Mn-Sn. J Appl Phys 2012;112:2010–5. https://doi.org/10.1063/1.4757425.
[15] Fukushima K, Sano K, Kanomata T, Nishihara H, Furutani Y, Shishido T, et al. Phase diagram of Fe-substituted Ni-Mn-Sn shape memory alloys. Scr Mater 2009;61:813–6. https://doi.org/10.1016/j.scriptamat.2009.07.003.
[16] Krenke T, Duman E, Acet M, Moya X, Mañosa L, Planes A. Effect of Co and Fe on the inverse magnetocaloric properties of Ni-Mn-Sn. J Appl Phys 2007;102:33903. https://doi.org/10.1063/1.2761853.
[17] Bachaga T, Daly R, Suñol JJ, Saurina J, Escoda L, Legarreta LG, et al. Effects of Co Additions on the Martensitic Transformation and Magnetic Properties of Ni–Mn–Sn Shape Memory Alloys. J Supercond Nov Magn 2015;28:3087–92. https://doi.org/10.1007/s10948-015-3100-z.
[18] Jing C, Li Z, Zhang HL, Chen JP, Qiao YF, Cao SX, et al. Martensitic transition and inverse magnetocaloric effect in Co doping Ni-Mn-Sn Heulser alloy. Eur Phys J B 2009;67:193–6. https://doi.org/10.1140/epjb/e2009-00023-9.
[19] Aguilar-Ortiz CO, Soto-Parra D, Álvarez-Alonso P, Lázpita P, Salazar D, Castillo-Villa PO, et al. Influence of Fe doping and magnetic field on martensitic transition in Ni-Mn-Sn melt-spun ribbons. Acta Mater 2016;107:9–16. https://doi.org/10.1016/j.actamat.2016.01.041.
[20] Passamani EC, Xavier F, Favre-Nicolin E, Larica C, Takeuchi AY, Castro IL, et al. Magnetic properties of NiMn-based Heusler alloys influenced by Fe atoms replacing Mn. J Appl Phys 2009;105:0–8. https://doi.org/10.1063/1.3075835.
[21] Wu Z, Liu Z, Yang H, Liu Y, Wu G, Woodward RC. Metallurgical origin of the effect of Fe doping on the martensitic and magnetic transformation behaviours of Ni50Mn40-xSn 10Fex magnetic shape memory alloys. Intermetallics 2011;19:445–52. https://doi.org/10.1016/j.intermet.2010.10.010.
[22] Tanaka Y, Ohmori T, Oikawa K, Kainuma R, Ishida K. Ferromagnetic Co-Ni-Al Shape Memory Alloys with β+γ Two-Phase Structure. Mater Trans 2004;45:427–30. https://doi.org/10.2320/matertrans.45.427.
[23] Santos JD, Sanchez T, Alvarez P, Sanchez ML, Sánchez Llamazares JL, Hernando B, et al. Microstructure and magnetic properties of Ni 50 Mn 37 Sn 13 Heusler alloy ribbons. J Appl Phys CN - 0000 2008;103:07B326. https://doi.org/10.1063/1.2832330.
[24] Khovaylo V V., Rodionova V V., Shevyrtalov SN, Novosad V. Magnetocaloric effect in

"reduced" dimensions: Thin films, ribbons, and microwires of Heusler alloys and related compounds. Phys Status Solidi Basic Res 2014;251:2104–13. https://doi.org/10.1002/pssb.201451217.
[25] Álvarez-Alonso P, Aguilar-Ortiz CO, Camarillo JP, Salazar D, Flores-Zúñiga H, Chernenko VA. Adiabatic magnetocaloric effect in Ni50Mn35In15 ribbons. Appl Phys Lett 2016;109. https://doi.org/10.1063/1.4968592.
[26] Hernando B, Llamazares JLS, Santos JD, Sánchez ML, Escoda L, Suñol JJ, et al. Grain oriented NiMnSn and NiMnIn Heusler alloys ribbons produced by melt spinning: Martensitic transformation and magnetic properties. J Magn Magn Mater 2009;321:763–8. https://doi.org/10.1016/j.jmmm.2008.11.105.
[27] Zhang H, Qian M, Zhang X, Wei L, Cao F, Xing D, et al. Martensite transformation and magnetic properties of Fe-doped Ni-Mn-Sn alloys with dual phases. J Alloys Compd 2016;689:481–8. https://doi.org/10.1016/j.jallcom.2016.07.282.
[28] Tan C, Tai Z, Zhang K, Tian X, Cai W. Simultaneous enhancement of magnetic and mechanical properties in Ni-Mn-Sn alloy by Fe doping. Sci Rep 2017;7:43387. https://doi.org/10.1038/srep43387.
[29] Sánchez Llamazares JL, Flores-Zúñiga H, Ríos-Jara D, Sánchez-Valdes CF, García-Fernández T, Ross CA, et al. Structural and magnetic characterization of the intermartensitic phase transition in NiMnSn Heusler alloy ribbons. J Appl Phys 2013;113:2013–6. https://doi.org/10.1063/1.4800836.
[30] Zhao XG, Tong M, Shih CW, Li B, Chang WC, Liu W, et al. Microstructure, martensitic transitions, magnetocaloric, and exchange bias properties in Fe-doped Ni-Mn-Sn melt-spun ribbons. J Appl Phys 2013;113:2012–5. https://doi.org/10.1063/1.4794881.
[31] Hernando B, Sánchez Llamazares JL, Santos JD, Prida VM, Baldomir D, Serantes D, et al. Magnetocaloric effect in melt spun Ni50.3 Mn35.5 Sn14.4 ribbons. Appl Phys Lett 2008;92:2012–5. https://doi.org/10.1063/1.2904625.
[32] Koyama K, Watanabe K, Kanomata T, Kainuma R, Oikawa K, Ishida K. Observation of field-induced reverse transformation in ferromagnetic shape memory alloy Ni50Mn36Sn14. Appl Phys Lett 2006;88:2004–7. https://doi.org/10.1063/1.2189916.
[33] Koyama K, Kanomata T, Kainuma R, Oikawa K, Ishida K, Watanabe K. High-field X-ray diffraction measurements of novel ferromagnetic shape-memory alloy Ni50Mn36Sn14. Phys B Condens Matter 2006;383:24–5. https://doi.org/10.1016/j.physb.2006.03.040.
[34] Chernenko VA. Compositional instability of β-phase in Ni-Mn-Ga alloys. Scr Mater 1999;42:523–7. https://doi.org/10.1016/S1359-6462(98)00494-1.
[35] Han ZD, Wang DH, Zhang CL, Xuan HC, Zhang JR, Gu BX, et al. Effect of lattice contraction on martensitic transformation and magnetocaloric effect in Ge doped Ni-Mn-Sn alloys. Mater Sci Eng B Solid-State Mater Adv Technol 2009;157:40–3. https://doi.org/10.1016/j.mseb.2008.12.006.
[36] Siewert M, Gruner ME, Hucht A, Herper HC, Dannenberg A, Chakrabarti A, et al. A first-principles investigation of the compositional dependent properties of magnetic shape memory heusler alloys. Adv Eng Mater 2012;14:530–46. https://doi.org/10.1002/adem.201200063.
[37] Wang X, Shang JX, Wang FH, Jiang CB, Xu H Bin. Effect of 3d transition elements substitution for Ni in Ni 2Mn1+xSn1-x on the phase stability and magnetic properties: A first principle investigation. J Magn Magn Mater 2014;368:286–94. https://doi.org/10.1016/j.jmmm.2014.05.040.
[38] Pathak AK, Dubenko I, Pueblo C, Stadler S, Ali N. Magnetoresistance and magnetocaloric effect at a structural phase transition from a paramagnetic martensitic state to a paramagnetic austenitic state in Ni50 Mn36.5 In13.5 Heusler alloys. Appl Phys Lett 2010;96. https://doi.org/10.1063/1.3422483.
[39] Zhukov A, Ipatov M, del Val JJ, Churyukanova M, Zhukova V. Tailoring of magnetic

properties of Heusler-type glass-coated microwires by annealing. J Alloys Compd 2018;732:561–6. https://doi.org/10.1016/j.jallcom.2017.10.232.
[40] Xuan HC, Cao QQ, Zhang CL, Ma SC, Chen SY, Wang DH, et al. Large exchange bias field in the Ni-Mn-Sn Heusler alloys with high content of Mn. Appl Phys Lett 2010;96:2010–3. https://doi.org/10.1063/1.3428782.
[41] Garcia C, Zhukova V, Shevyrtalov S, Ipatov M, Corte-Leon P, Zhukov A. Tuning of magnetic properties in Ni-Mn-Ga Heusler-type glass-coated microwires by annealing. J Alloys Compd 2020;838:155481. https://doi.org/10.1016/j.jallcom.2020.155481.
[42] Peleg N, Shtrikman S, Gorodetsky G, Felner I. Magnetic study of particle distribution in granular AuCo. J Magn Magn Mater 1999;191:349–53. https://doi.org/10.1016/S0304-8853(98)00337-0.
[43] Denardin JC, Brandl AL, Knobel M, Panissod P, Pakhomov AB, Liu H, et al. Thermoremanence and zero-field-cooled/field-cooled magnetization study of (formula presented) granular films. Phys Rev B - Condens Matter Mater Phys 2002;65:1–8. https://doi.org/10.1103/PhysRevB.65.064422.
[44] Czaja P, Fitta M, Przewoźnik J, Maziarz W, Morgiel J, Czeppe T, et al. Effect of heat treatment on magnetostructural transformations and exchange bias in Heusler Ni48Mn39.5Sn9.5Al3ribbons. Acta Mater 2016;103:30–45. https://doi.org/10.1016/j.actamat.2015.10.001.
[45] Koyama K, Igarashi T, Okada H, Watanabe K, Kanomata T, Kainuma R, et al. Magnetic and thermoelectric properties of Ni50Mn36Sn14 in high-magnetic fields. J Magn Magn Mater 2007;310:994–5. https://doi.org/10.1016/j.jmmm.2006.10.1040.
[46] Liao P, Jing C, Zheng D, Li Z, Kang B, Deng D, et al. Tuning martensitic transformation, large magnetoresistance and strain in Ni50-xFexMn36Sn14 Heusler alloys. Solid State Commun 2015;217:28–33. https://doi.org/10.1016/j.ssc.2015.05.012.
[47] Zhukova V, Ipatov M, Talaat A, Zhukov A. Hopkinson effect in Co-rich glass-coated microwires. Phys Status Solidi Curr Top Solid State Phys 2014;11:1130–2. https://doi.org/10.1002/pssc.201300715.
[48] Buzinaro MAP, Ferreira NS, Cunha F, MacÊdo MA. Hopkinson effect, structural and magnetic properties of M-type Sm3+-doped SrFe12O19 nanoparticles produced by a proteic sol-gel process. Ceram Int 2016;42:5865–72. https://doi.org/10.1016/j.ceramint.2015.12.130.
[49] Pozo-López G, Condó AM, Fabietti LM, Winkler E, Haberkorn N, Urreta SE. Microstructure of as-cast single and twin roller melt-spun Ni2MnGa ribbons. Mater Charact 2017;124:171–81. https://doi.org/10.1016/j.matchar.2016.12.020.
[50] S. UB, Choudary GSVRK, Reddy MVR. Modulation in magnetic exchange interaction, core shell structure and Hopkinson's peak with chromium substitution into Ni0.75Co0.25Fe2O4 nano particles. J Magn Magn Mater 2018;454:349–55. https://doi.org/10.1016/j.jmmm.2018.01.093.
[51] Coey JMD. Magnetism and magnetic materials, New York: Cambridge University Press; 2009, p. 273–4.
[52] He K, Xu H, Wang Z, Cheng L. Hopkinson effect in soft magnetic materials. J Mater Sci Technol 2000;16:145–7.
[53] Castillo-Villa PO, Mañosa L, Planes A, Soto-Parra DE, Sánchez-Llamazares JL, Flores-Zúñiga H, et al. Elastocaloric and magnetocaloric effects in Ni-Mn-Sn(Cu) shape-memory alloy. J Appl Phys 2013;113:053506. https://doi.org/10.1063/1.4790140.
[54] Emre B, Bruno NM, Emre SY, Karaman I. Effect of niobium addition on the martensitic transformation and magnetocaloric effect in low hysteresis NiCoMnSn magnetic shape memory alloys. Appl Phys Lett 2014;105:5–10. https://doi.org/10.1063/1.4903494.
[55] Marcano N, Algarabel PA, Barquín LF, Araujo JP, Pereira AM, Belo JH, et al. Cluster-glass dynamics of the Griffiths phase in Tb5-xLaxSi2Ge2. Phys Rev B 2019;99:1–10.

https://doi.org/10.1103/PhysRevB.99.054419.
[56] Samanta T, Bhobe PA, Das A, Kumar A, Nigam AK. Reentrant cluster glass and stability of ferromagnetism in the Ga2MnCo Heusler alloy. Phys Rev B 2018;97:1–7. https://doi.org/10.1103/PhysRevB.97.184421.
[57] Khan M, Dubenko I, Stadler S, Ali N. Exchange bias behavior in Ni-Mn-Sb Heusler alloys. Appl Phys Lett 2007;91:23–5. https://doi.org/10.1063/1.2772233.
[58] López Antón R, González JA, Andrés JP, Normile PS, Muñiz P, Riveiro JM, et al. Exchange Bias Optimization by Controlled Oxidation of Cobalt Nanoparticle Films Prepared by Sputter Gas Aggregation. Nanomaterials 2017;7:1–9. https://doi.org/10.3390/nano7030061.
[59] Zhang J, Zhao W, Feng Z, Ge JY, Zhang J, Cao S. Spin reorientation and rare earth antiferromagnetic transition in single crystal Sm0.15Dy0.85FeO3. J Alloys Compd 2019;804:396–400. https://doi.org/10.1016/j.jallcom.2019.07.035.
[60] Nayak AK, Suresh KG, Nigam AK. Observation of enhanced exchange bias behaviour in NiCoMnSb Heusler alloys. J Phys D Appl Phys 2009;42. https://doi.org/10.1088/0022-3727/42/11/115004.
[61] Khan M, Albagami A. Cooling field dependent exchange bias in Mn 2 Ni 1.4 Ga 0.6 : A reentrant spin glass system with short range ferromagnetic ordering. J Alloys Compd 2017;727:100–6. https://doi.org/10.1016/j.jallcom.2017.08.112.
[62] Brück S, Sort J, Baltz V, Suriñach S, Muñoz JS, Dieny B, et al. Exploiting length scales of exchange-bias systems to fully tailor double-shifted hysteresis loops. Adv Mater 2005;17:2978–83. https://doi.org/10.1002/adma.200500544.
[63] Jia J, Chen Y, Wang B, Han B, Wu Y, Wang Y, et al. The double-shifted magnetic hysteresis loops and domain structure in perpendicular [Co/Ni]N/IrMn exchange biased systems. J Phys D Appl Phys 2019;52:aaf0f9. https://doi.org/10.1088/1361-6463/aaf0f9.
[64] Chernenko VA, Barandiarán JM, Rodriguez Fernández J, Rojas DP, Gutiérrez J, Lázpita P, et al. Magnetic and magnetocaloric properties of martensitic Ni 2Mn 1.4Sn 0.6 Heusler alloy. J Magn Magn Mater 2012;324:3519–23. https://doi.org/10.1016/j.jmmm.2012.02.080.
[65] Pathak AK, Khan M, Gautam BR, Stadler S, Dubenko I, Ali N. Exchange bias in bulk Ni-Mn-In-based Heusler alloys. J Magn Magn Mater 2009;321:963–5. https://doi.org/10.1016/j.jmmm.2008.03.008.
[66] Pathak A, Dubenko I. Exchange bias in bulk Ni Mn In Si Heusler alloys. IEEE Trans Magn 2009;45:3855–7.
[67] Ali M, Adie P, Marrows CH, Greig D, Hickey BJ, Stamps RL. Exchange bias using a spin glass. Nat Mater 2007;6:70–5. https://doi.org/10.1038/nmat1809.
[68] Han X, Chen C, Ma S, Zhang Z, Liu K, Song Y, et al. Microstructure, magnetic properties, and exchange bias in (Mn0.7Co0.3)65Sn35 alloy ribbons. J Magn Magn Mater 2019;492:165686. https://doi.org/10.1016/j.jmmm.2019.165686.
[69] Khovaylo V V., Skokov KP, Gutfleisch O, Miki H, Kainuma R, Kanomata T. Reversibility and irreversibility of magnetocaloric effect in a metamagnetic shape memory alloy under cyclic action of a magnetic field. Appl Phys Lett 2010;97:2010–3. https://doi.org/10.1063/1.3476348.
[70] Li Z, Yang J, Li D, Li Z, Yang B, Yan H, et al. Tuning the Reversible Magnetocaloric Effect in Ni–Mn–In-Based Alloys through Co and Cu Co-Doping. Adv Electron Mater 2019;5:1–9. https://doi.org/10.1002/aelm.201800845.
[71] Zverev VI, Saletsky AM, Gimaev RR, Tishin AM, Miyanaga T, Staunton JB. Influence of structural defects on the magnetocaloric effect in the vicinity of the first order magnetic transition in Fe50.4Rh49.6. Appl Phys Lett 2016;108:1–6. https://doi.org/10.1063/1.4949355.
[72] Chirkova A, Skokov KP, Schultz L, Baranov N V., Gutfleisch O, Woodcock TG. Giant

adiabatic temperature change in FeRh alloys evidenced by direct measurements under cyclic conditions. Acta Mater 2016;106:15–21. https://doi.org/10.1016/j.actamat.2015.11.054.

[73] Quintana-Nedelcos A, Llamazares JLS, Ríos-Jara D, Lara-Rodríguez AG, García-Fernández T. Effect of quenching rate on the average grain size and martensitic transformation temperature in rapidly solidified polycrystalline Ni 50Mn37Sn13 alloy ribbons. Phys Status Solidi Appl Mater Sci 2013;210:2159–65. https://doi.org/10.1002/pssa.201329146.

[74] Khovailo V V., Oikawa K, Abe T, Takagi T. Entropy change at the martensitic transformation in ferromagnetic shape memory alloys Ni2+xMn1-xGa. J Appl Phys 2003;93:8483–5. https://doi.org/10.1063/1.1556218.

[75] Khovailo V V., Takagi T, Tani J, Levitin RZ, Cherechukin AA, Matsumoto M, et al. Magnetic properties of (formula presented)Ga Heusler alloys with a coupled magnetostructural transition. Phys Rev B - Condens Matter Mater Phys 2002;65:1–4. https://doi.org/10.1103/PhysRevB.65.092410.

TABLES CAPTIONS

Table 1. Chemical composition, with an uncertainty of 0.5 at. %, cell parameters, and lattice volume of the cubic and orthorhombic phases and the transformation volume for $Ni_{50}Mn_{36-x}Sn_{14}Fe_x$ melt-spun ribbons for the martensite and austenite phases.

Table 2. Starting, T_{AS} and T_{MS}, finishing, T_{AF} and T_{MF}, and peak, T_A and T_M, temperatures, thermal hysteresis, enthalpy and entropy of the forward and reverse MT, and equilibrium temperature T_0 obtained from the DSC data, and Curie temperature of the austenite and martensite estimated from ZFC curves.

Table 3. Elastic and dissipated energy of the direct and reverse structural transformation.

FIGURE CAPTIONS

Figure 1. Scanning electron micrographs of the ribbons cross-section for samples (a) Fe0, (b) Fe 2, and (c) Fe3.

Figure 2. DSC Thermograms for the studied ribbons.

Figure 3. X-ray powder diffraction patterns of the Fe0 (a) specimen collected at 350 K and of the Fe2 (b) and Fe3 (c) ribbons collected at 295 K. Miller indexes are included to ease the reader the identification of structures. Reflections corresponding to the sample holder and to the 4O phase (present in the Fe2 sample) are indicated by SH and 4O respectively. The reflections of the 4O phase have been Miller indexed. Where sample holder and crystal structure peaks overlap, both peaks are shown with a plus (+) symbol.

Figure 4. X-ray powder diffraction patterns recorded at 150 K for (a) x=0, (b) x=2, and (c) x=3. Miller indexes are included to ease the reader the identification of structures. Reflections corresponding to the sample holder are indicated by SH. Where sample holder and crystal structure peaks overlap, both peaks are shown with a plus (+) symbol.

Figure 3. Magnetization vs temperature curves for the (a) Fe0, (b) Fe2, and (c) Fe3 samples under an applied magnetic field of 5 mT and 3 T, measured under the ZFC (blue squares), FC (red triangles), and FH (black circles) protocols

Figure 6. Heating magnetization curves obtained under different applied magnetic fields for specimen Fe3.

Figure 7. Temperature dependence of the real part (left hand, (a) Fe0, (c) Fe2, (e) Fe3) and imaginary part (right hand, (b) Fe0, (d) Fe2, (f) Fe3) of the AC magnetic susceptibility AC magnetic susceptibility of all the samples, measured with an ac field of 0.35 mT and different ac frequencies and in heating or cooling regime: 100 Hz, heating (black points); 10 kHz, cooling (red points); and 10kHz, heating (green points)

Figure 8. Hysteresis loops of the samples obtained at 2 K FC (solid circles) and ZFC (empty squares) protocols (left). Evolution of the coercivity (black squares) and exchange field (empty blue circles) with the temperature, obtained under FC protocol.

Figure 9. Variation of the total entropy of the martensitic transformation vs T_C^A-T_0. Black curve shows the fit to an exponential function.

Figure 10. Magnetic entropy change as a function of the temperature for a magnetic field change 0-3 T for the studied ribbons. Inset: temperature dependence of the magnetic entropy change for the Fe2 specimen obtained from the magnetization measured under the ZFC thermal protocol.

TABLES

Table 1. Chemical composition, with an uncertainty of 0.5 at. %, cell parameters, and lattice volume of the cubic and orthorhombic phases and the transformation volume for $Ni_{50}Mn_{36-x}Sn_{14}Fe_x$ melt-spun ribbons for the martensite and austenite phases.

Nominal composition	Chemical composition	*e/a*	a_A (Å)	V_A (Å^3)	a_M (Å)	b_M (Å)	c_M (Å)	V_M (Å^3)	$\Delta V/V$ (%)
$Ni_{50}Mn_{36}Sn_{14}$	$Ni_{53.0}Mn_{33.0}Sn_{14.0}$	8.17	5.96(9)	213	8.57(1)	5.64(3)	4.32(8)	209	-1.9
$Ni_{50}Mn_{34}Sn_{14}Fe_2$	$Ni_{52.0}Mn_{31.5}Sn_{14.5}Fe_{2.0}$	8.15	5.96(9)	212	8.56(9)	5.64(2)	4.36(5)	211	-0.5
$Ni_{50}Mn_{33}Sn_{14}Fe_3$	$Ni_{51.5}Mn_{31.0}Sn_{14.5}Fe_{3.0}$	8.14	5.97(5)	213	8.61(5)	5.62(4)	4.37(1)	212	-0.5

Table 2. Starting, T_{AS} and T_{MS}, finishing, T_{AF} and T_{MF}, and peak, T_A and T_M, temperatures, thermal hysteresis, enthalpy and entropy of the forward and reverse MT, and equilibrium temperature T_0 obtained from the DSC data, and Curie temperature of the austenite and martensite estimated from ZFC curves.

x	T_{AS} (K)	T_{AF} (K)	T_A (K)	T_C^A (K)	T_{MS} (K)	T_{MF} (K)	T_M (K)	T_{C1}^M (K)	T_{C2}^M (K)	ΔT (K)	T_0 (K)	$\lvert\Delta H_A\rvert$ (Jg^{-1})	$\lvert\Delta S_A\rvert$ (Jkg^{-1}K^{-1})	ΔH_M (Jg^{-1})	ΔS_M (Jkg^{-1}K^{-1})
0	327	344	335	336	326	315	320	303	206	15	328	14.4	43.9	13.1	39.9
2	298	309	305	306	298	286	293	288	225	12	300	13.1	43.7	17.6	58.7
3	286	294	291	300	282	274	278	289	240	13	285	9.8	34.4	11.2	39.3

Table 3. Elastic and dissipated energy of the direct and reverse structural transformation.

Elastic/dissipated energy	Fe0	Fe2	Fe3
Accumulated elastic energy from Austenitic transformation ($E_{el}/\Delta H_A$) (%)	2.166	1.949	1.434
Irreversibly dissipated energy from Austenitic transformation ($W_d/\Delta H_A$) (%)	4.592	3.888	4.316
Accumulated elastic energy from Martensitic transformation ($E_{el}/\Delta H_M$) (%)	2.271	2.045	1.498
Irreversibly dissipated energy from Martensitic transformation ($W_d/\Delta H_M$) (%)	4.814	4.082	4.509

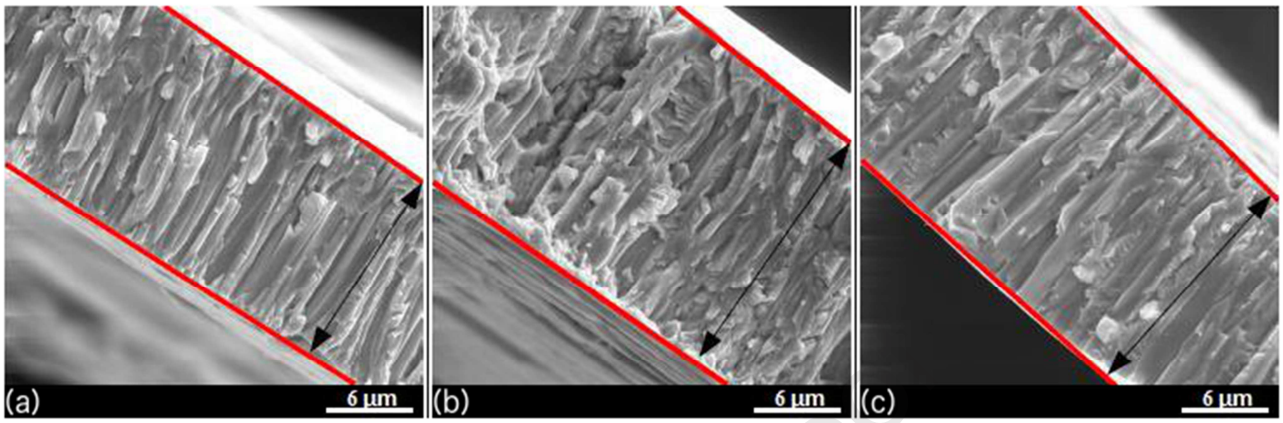

Figure 1. Scanning electron micrographs of the ribbons cross-section for samples (a) Fe0, (b) Fe 2, and (c) Fe3.

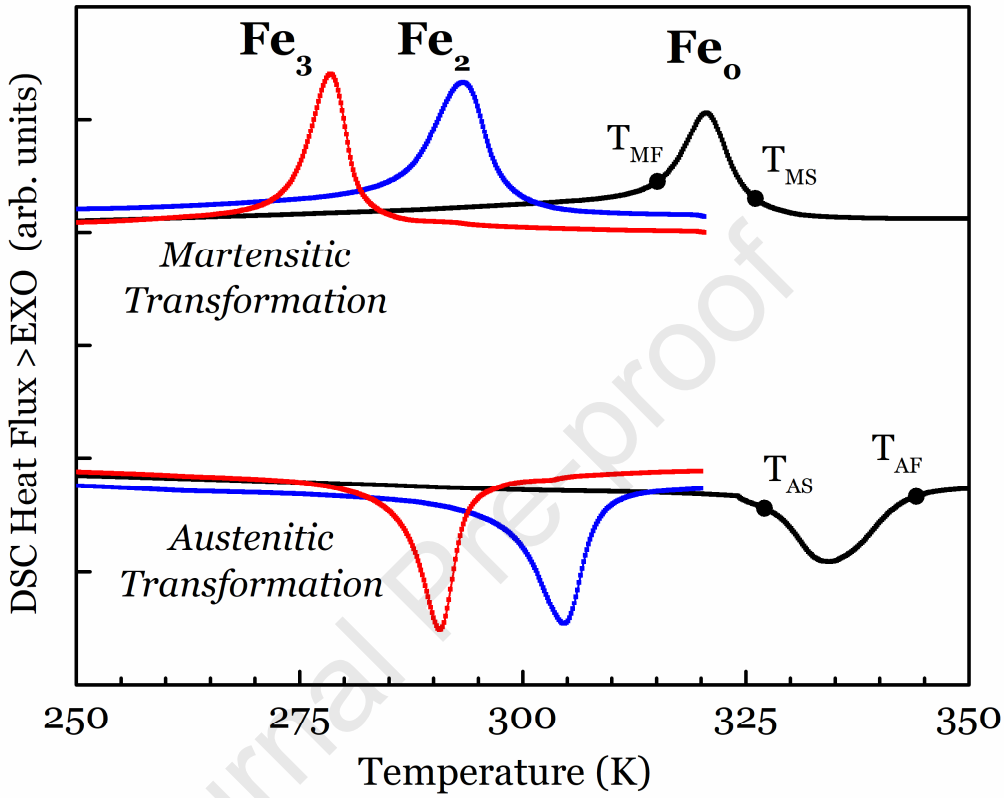

Figure 2. DSC Thermograms for the studied ribbons.

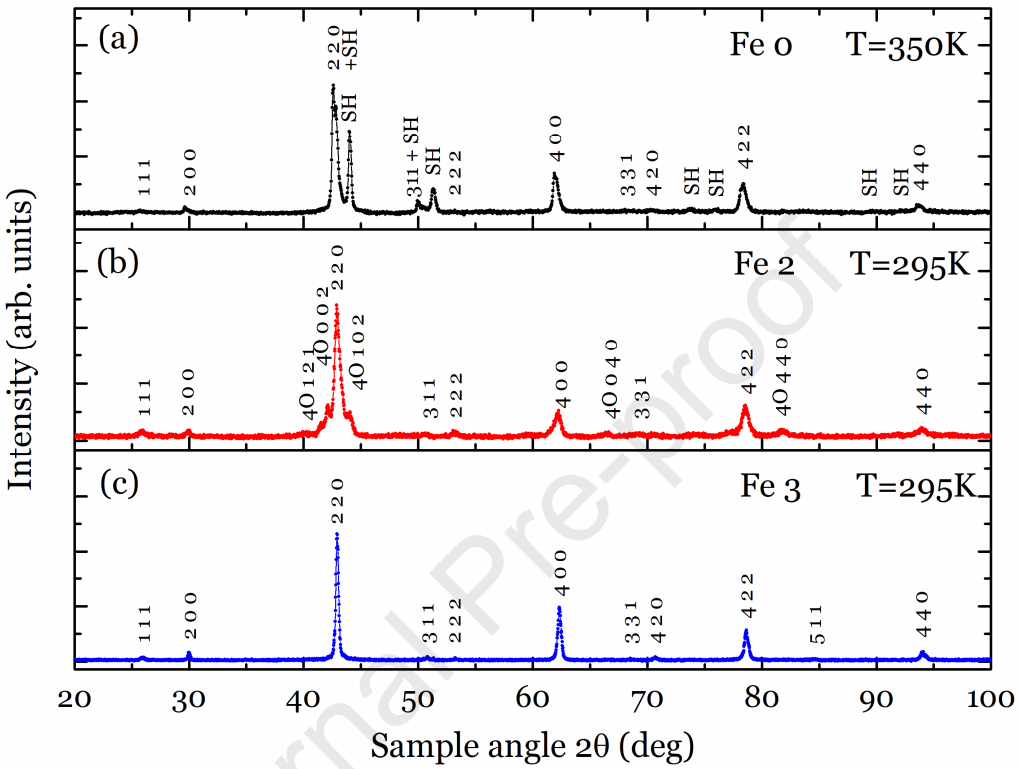

Figure 3. X-ray powder diffraction patterns of the Fe0 (a) specimen collected at 350 K and of the Fe2 (b) and Fe3 (c) ribbons collected at 295 K. Miller indexes are included to ease the reader the identification of structures. Reflections corresponding to the sample holder and to the 4O phase (present in the Fe2 sample) are indicated by SH and 4O respectively. The reflections of the 4O phase have been Miller indexed. Where sample holder and crystal structure peaks overlap, both peaks are shown with a plus (+) symbol.

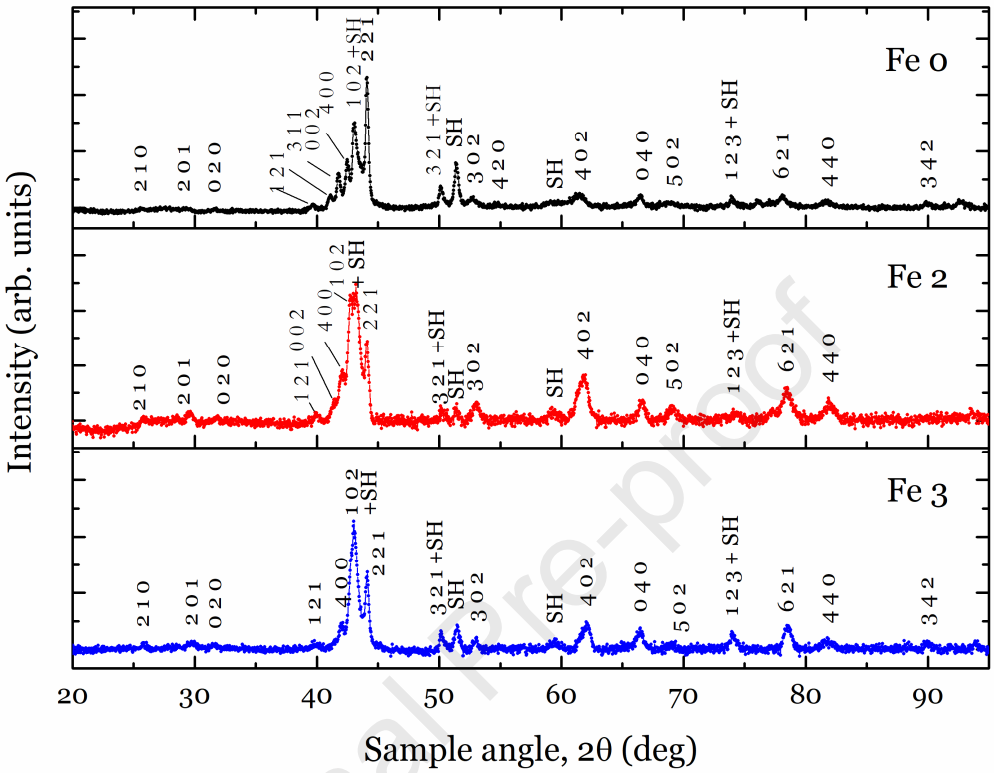

Figure 4. X-ray powder diffraction patterns recorded at 150 K for (a) x=0, (b) x=2, and (c) x=3. Miller indexes are included to ease the reader the identification of structures. Reflections corresponding to the sample holder are indicated by SH. Where sample holder and crystal structure peaks overlap, both peaks are shown with a plus (+) symbol.

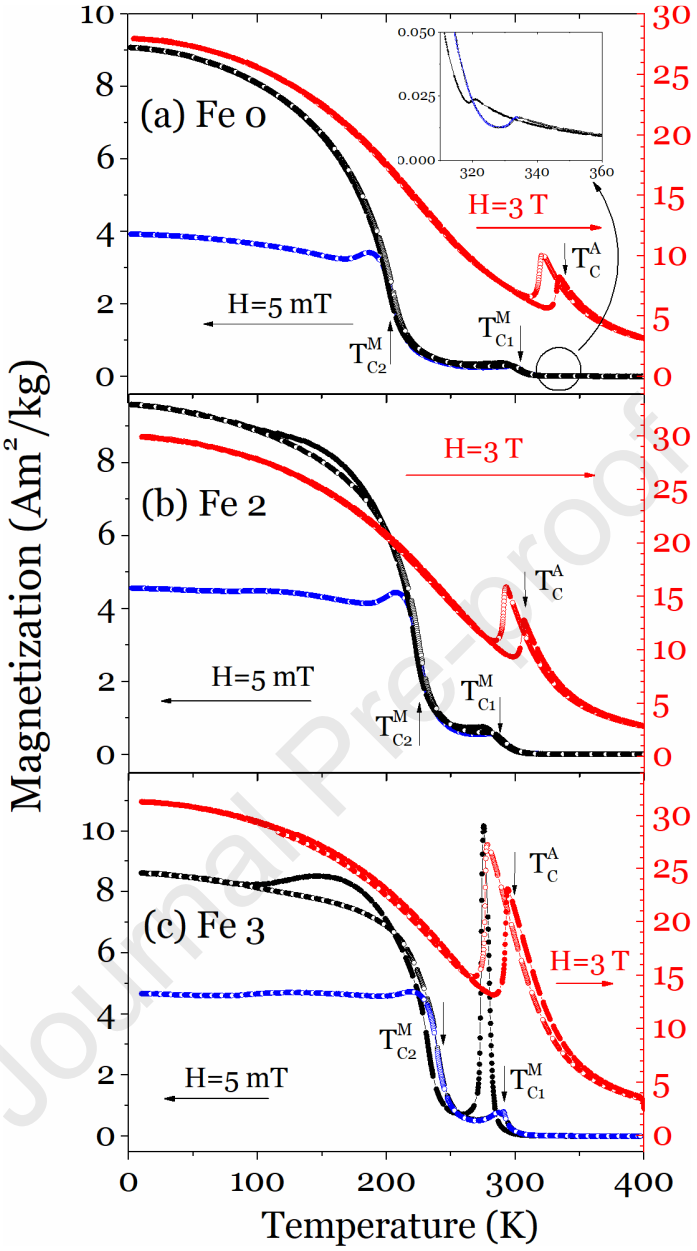

Figure 4. Magnetization vs temperature curves for the (a) Fe0, (b) Fe2, and (c) Fe3 samples under an applied magnetic field of 5 mT and 3 T, measured under the ZFC (blue squares), FC (red triangles), and FH (black circles) protocols

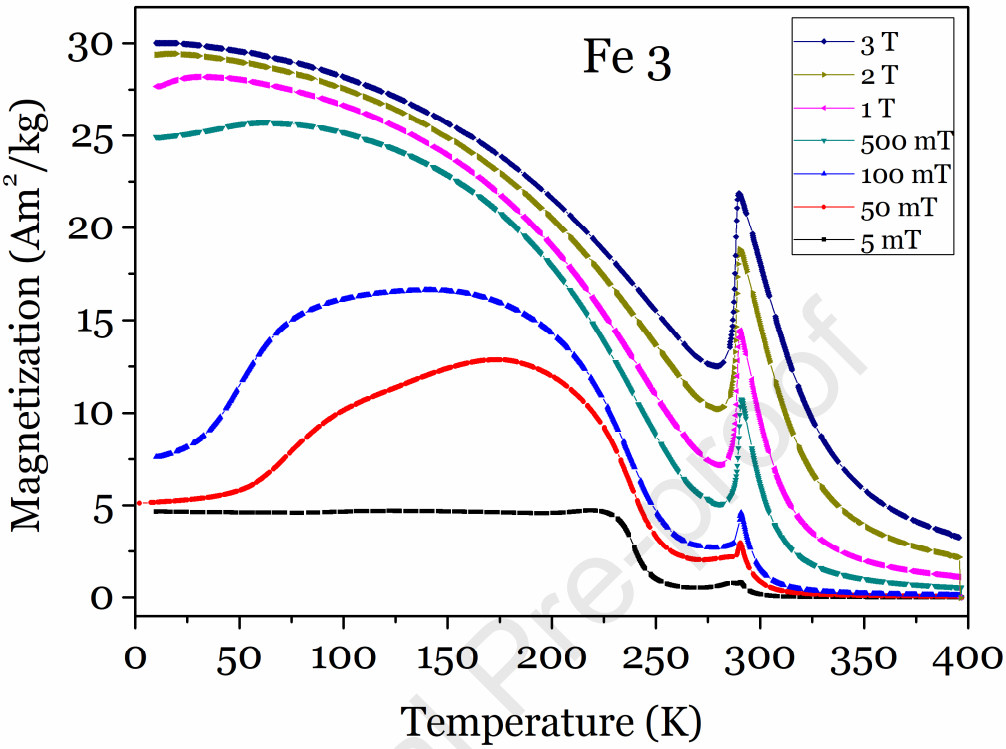

Figure 6. Heating magnetization curves obtained under different applied magnetic fields for specimen Fe3.

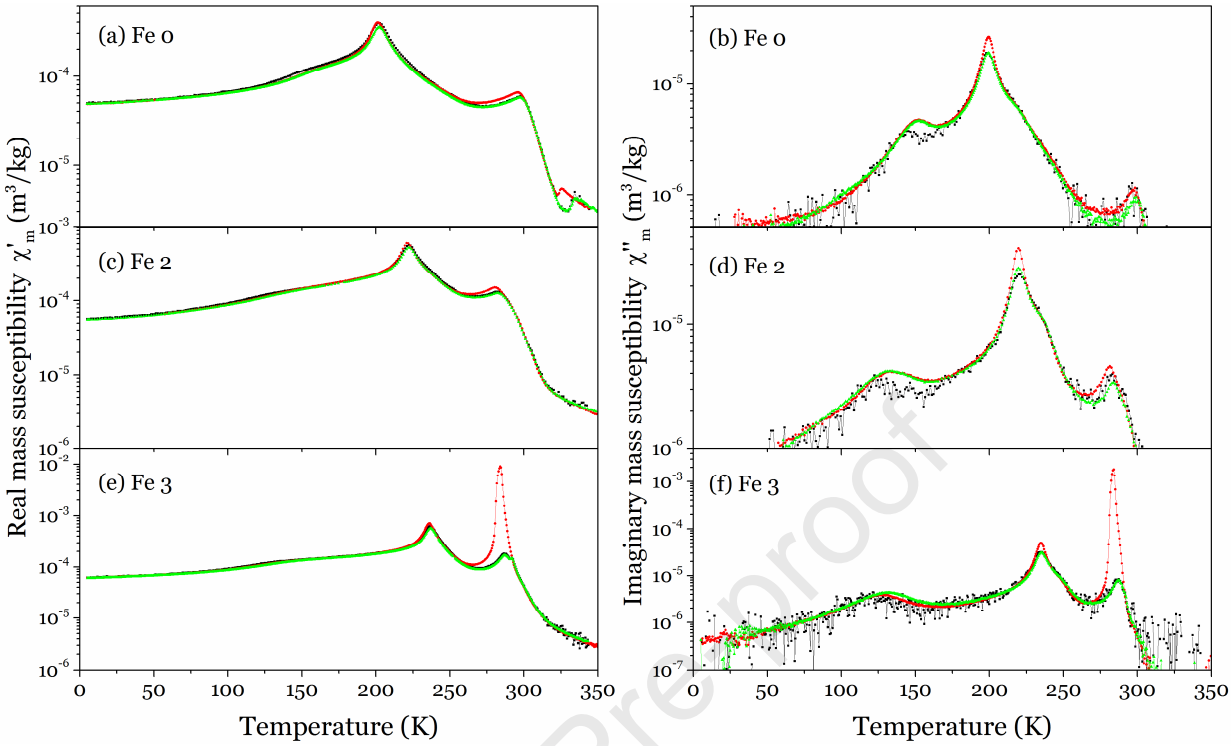

Figure 7. Temperature dependence of the real part (left hand, (a) Fe0, (c) Fe2, (e) Fe3) and imaginary part (right hand, (b) Fe0, (d) Fe2, (f) Fe3) of the AC magnetic susceptibility AC magnetic susceptibility of all the samples, measured with an ac field of 0.35 mT and different ac frequencies and in heating or cooling regime: 100 Hz, heating (black points); 10 kHz, cooling (red points); and 10kHz, heating (green points)

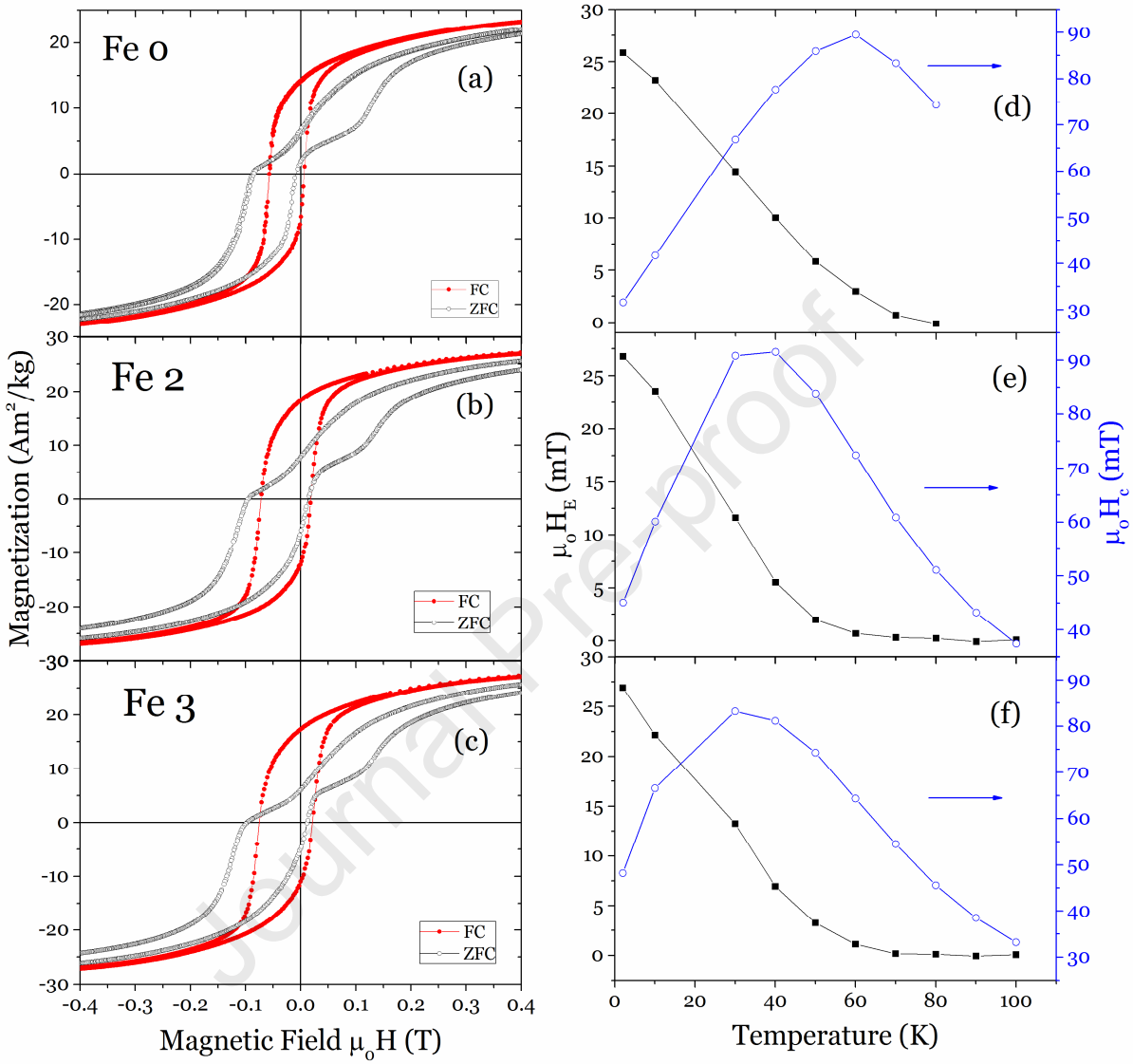

Figure 8. Hysteresis loops of the samples obtained at 2 K FC (solid circles) and ZFC (empty squares) protocols (left). Evolution of the coercivity (black squares) and exchange field (empty blue circles) with the temperature, obtained under FC protocol.

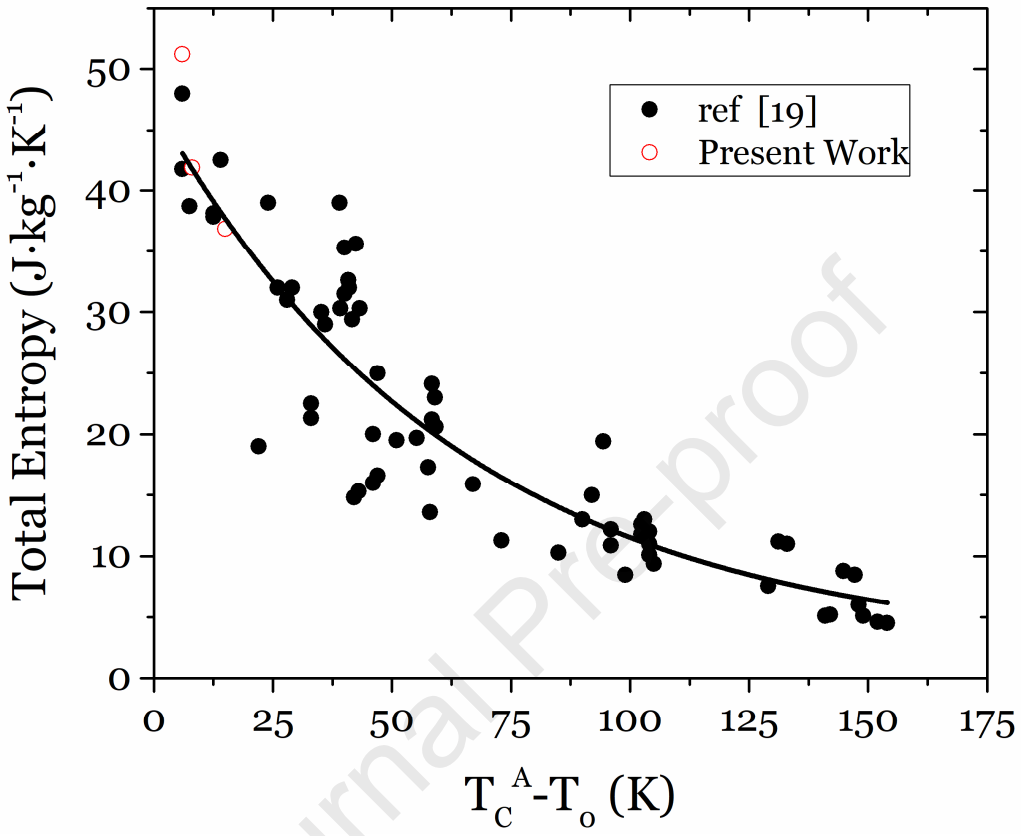

Figure 9. Variation of the total entropy of the martensitic transformation vs T_C^A-T_0. Black curve shows the fit to an exponential function.

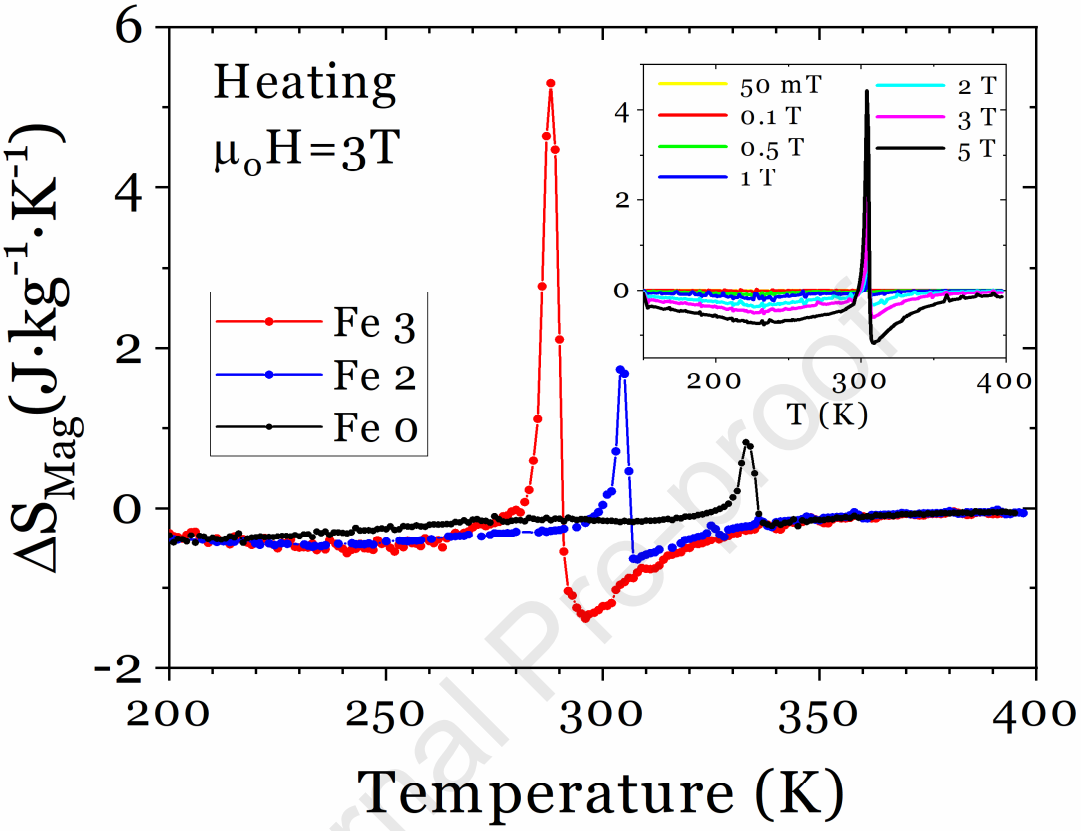

Figure 10. Magnetic entropy change as a function of the temperature for a magnetic field change 0-3 T for the studied ribbons. Inset: temperature dependence of the magnetic entropy change for the Fe2 specimen obtained from the magnetization measured under the ZFC thermal protocol.

Declaration of interests

☒ The authors declare that they have no known competing financial interests or personal relationships that could have appeared to influence the work reported in this paper.

☐The authors declare the following financial interests/personal relationships which may be considered as potential competing interests: